An improved direct-forcing immersed-boundary method for finite difference applications

N. Zhang, Z.C. Zheng *

Department of Mechanical and Nuclear Engineering, Kansas State University, Manhattan, KS 66506-5205, USA

Abstract

A modified immersed-boundary method is developed using the direct-forcing concept. An improved bilinear interpolation/extrapolation algorithm is implemented for more accurate boundary forcing expressions and easier implementation. Detailed discussions of the method are presented on the stability, velocity interpolation on the immersed boundary, direct-forcing extrapolation to the grid points, resolution of the immersed boundary points, and internal treatment. The method can achieve second-order accurate solutions. The method is then applied to a finite-difference scheme to compute flow over a stationary cylinder, an oscillating cylinder, and a stationary sphere. The accuracy of the computational results is verified using numerous computational and experimental results in the literature.
© 2006 Elsevier Inc. All rights reserved.

1. Introduction

This paper describes an immersed boundary-like approach to modeling and simulating flow over a cylinder and a sphere. Immersed boundary (IB) methods for fluid-structure interaction problems typically discretize the equations of motion for the fluid (in this case, the incompressible Navier–Stokes equations) on a Cartesian grid, and such methods generally do not require that the geometry of the structure conform in any way to this Cartesian grid. Instead, the equations of motion for the fluid are augmented by an appropriately defined forcing term that typically is nonzero only in the vicinity of the structure.

The IB methods were first applied by Peskin [13] to flow around the flexible leaflet of a human heart. The IB provided the advantage to solve the Navier–Stokes equations on a single rectangular domain where the flexible boundaries were enabled to move or change shapes in a complicated fashion. More recent development and reviews of IB methods with elastic boundaries are in [8,14].

---

* Corresponding author. Tel.: +1 785 5325610; fax: +1 785 5327057.
E-mail address: zzheng@ksu.edu (Z.C. Zheng).

For the class of problems considered in the present work, the structure is rigid (i.e., the boundary is fixed) and the velocity on the body surface is specified, so the forcing term is used to approximately enforce velocity boundary conditions on the body. Such methods are also known as virtual boundary methods. Goldstein et al. [4] developed a feedback-force IB method for the virtual boundary problems. The forcing term was determined by integrating the velocity of the surface points with two negative constants. The two negative constants were obtained semi-empirically that usually imposed restrictive stability conditions on the time step used in the computation. Again, all simulations could be performed on a Cartesian grid mesh, with no mapping of mesh needed to accommodate the solid boundary geometries. Saiki and Biringen [17] (referred as S&B hereafter) used this feedback-force IB method to calculate low Reynolds number ($Re \leqslant 400$) flow over a stationary, rotating and horizontally oscillating cylinder. They showed that the feedback-force IB method was capable of handling the solid boundary problems including also moving boundaries.

The feedback-force IB methods sometimes have severe stability problems, and therefore can be very expensive when used to simulate flow with complex 3-D geometries. A new IB method, named the direct-forcing IB method, was developed by Mohd-Yusof [11]. This method uses a forcing term determined by the difference between the interpolated velocities on the boundary points and the desired (physical) boundary velocities. The forcing term generated in this manner thus directly compensates the errors between the calculated velocities and the desired velocities on the boundary. The method employs a forcing term that is determined to "exactly" impose the desired velocity profile on the body surface [2]. With this method, the computation no longer suffers the stability limitation, and no empirical constants are needed to form the forcing term as in Goldstein et al.'s [4] scheme. The direct-forcing IB methods have been used successfully to simulate flow around the spherical particles in the particle–gas two-phase flow [11], 3-D complex flow problems [2,12] and flow with a moving object [22].

Recently, Ravoux et al. [15] proposed an embedding method that combined the IB method and the volume of fluid (VOF) method. Their method can be considered as a direct-forcing method and, like the previous IB methods, the presence of the solid body is represented by an external body force in the flow equations. The difference is that the force is determined using the VOF method. They applied the embedding IB method to study the flow past two side-by-side stationary cylinders. There are other direct-forcing methods with different ways of treating the IB conditions [18,21].

The purpose of this paper is to present an improved IB method that adapts the direct-forcing idea from Mohd-Yusof [11]. The difference from previous direct-forcing methods is in the interpolation of the velocity and the extrapolation of the body force. The current bilinear interpolation/extrapolation function is the same function introduced by S&B. The forcing term is the direct forcing instead of feedback forcing in S&B, and is applied to the internal layer (interior to the body) instead of both interior and exterior to the body in S&B. The advantages of using the S&B-type interpolation and extrapolation are: 1) it is easy for coding; 2) the number of boundary points can be increased independently to the computational grid, therefore the accuracy in the region near the boundary can be enhanced without using higher-order schemes, or arranging complicated grids near the boundary. These complicated boundary treatments include embedded grids such as those mentioned in [2], ghost cells [21], and Lagrangian points [18]. The current scheme obtains second-order accurate solutions via a method that is more easily implemented and less "*ad hoc*" than the second order accurate scheme detailed in [2], in the sense that a more easily implemented interpolation/extrapolation scheme is used on the IB. For validation cases, flow over a stationary cylinder, an oscillating cylinder, and a stationary sphere has been simulated. Evidences of good agreements in comparisons of the current computational results with previous numerical and experimental studies have been found for the steady and unsteady features in both of the near-field and far-field regions of the flow.

2. Description of the IB method

Since this paper follows the direct-forcing method in [11] and uses the interpolation/extrapolation procedures in [17], the methods in [11,17] are briefly summarized first. Then the current method is described and the differences and advantages of the method are discussed. Detailed discussions of the method are presented on the stability, velocity interpolation on the immersed boundary, direct-forcing extrapolation to the grid points, resolution of the immersed boundary points, and internal treatment.

2.1. The feedback-force method of Saiki and Biringen [17]

In the IB method, the equations for incompressible fluid flow are

$$\frac{\partial \mathbf{u}}{\partial t} + \mathbf{u} \cdot \nabla \mathbf{u} = -\nabla P + \frac{1}{Re} \nabla^2 \mathbf{u} + \mathbf{f} \tag{1}$$

and

$$\nabla \cdot \mathbf{u} = 0, \tag{2}$$

where $\mathbf{f}$ is the body force representing the virtual boundary force.

In the feedback-force IB method, the body force on each grid is determined by

$$\mathbf{f} = D(\mathbf{x}_s)\mathbf{F}(\mathbf{x}_s, t), \tag{3}$$

where $\mathbf{x}_s$ is the coordinates of the surface, D is the interpolation functions used to interpolate the force from the virtual boundary points to the grid points. The force $\mathbf{F}$ is expressed as

$$\mathbf{F}(\mathbf{x}_s, t) = \alpha \int_0^t [\mathbf{U}(\mathbf{x}_s, \tau) - \mathbf{V}(\mathbf{x}_s, \tau)]d\tau + \beta[\mathbf{U}(\mathbf{x}_s, t) - \mathbf{V}(\mathbf{x}_s, t)], \tag{4}$$

where $\mathbf{U}$ is the flow velocity on the surface, $\mathbf{V}$ is the velocity of the solid body motion (if the body is moving), and α and β are negative constants that are empirically determined.

In the spirit of the IB methods, the desired (physical) boundary velocity $\mathbf{V}$ is located on a boundary surface that need not coincide with the grid points. In S&B, the actual (computed) IB velocity $\mathbf{U}$ at the IB point, (x_s, y_s), is calculated by a bilinear interpolation from the four surrounding grid points denoted by indices (i,j), $(i+1,j)$, $(i,j+1)$ and $(i+1, j+1)$:

$$\mathbf{U}(\mathbf{x}_s) = \sum_{i,j}^{i+1,j+1} D_{i,j}(\mathbf{x}_s)\mathbf{u}_{i,j}^n, \tag{5}$$

where the weighting function $D_{i,j}$ is defined as:

$$D_{i,j}(\mathbf{x_s}) = d(x_s - x_i)\,d(y_s - y_i). \tag{6}$$

In Eq. (6), x_s and y_s are respectively the x and y locations of the IB point, and

$$d(x_s - x_i) = (x_s - x_{i+1})/(x_i - x_{i+1}) \quad \text{if } x_i < x_s,$$
$$d(x_s - x_i) = (x_s - x_{i-1})/(x_i - x_{i-1}) \quad \text{if } x_i > x_s,$$
$$d(x_s - x_i) = 1 \quad \text{if } x_i = x_s.$$

For example, if the IB point is at Point A shown in Fig. 1(a), then the (i,j) point is at Point 1. The computed velocity at Point A is interpolated by the velocities at Points 1–4 using Eq. (5).

In the feedback-force IB method in [17], $\mathbf{U}(\mathbf{x}_s)$ from Eq. (5) is substituted into Eq. (4) to form the force imposed at the IB points. Then the effect of this IB force is extrapolated back to the grid points by area-weighted averages that use the same weighting functions, $D_{i,j}$.

2.2. The direct-forcing method of Mohd-Yusof [11]

In the direct-forcing IB method, the governing equations for the incompressible flow are the same as Eqs. (1) and (2). However, a direct compensation force is used, instead of a feedback force of Eq. (4). The forcing term $\mathbf{f}$, which functions as a velocity corrector for the grid points immediately inside the IB, is prescribed at each time step to establish the desired boundary moving velocity $\mathbf{V}$. For a time-marching scheme, this force can be expressed as

$$\mathbf{f} = \mathbf{S} + \nabla P - \frac{1}{Re}\nabla^2 \mathbf{u} + \frac{1}{\Delta t}(\mathbf{v} - \mathbf{u}^n) \tag{7}$$
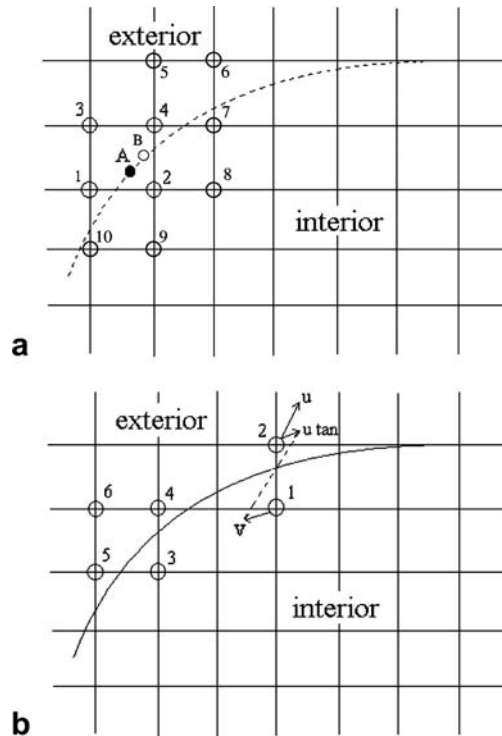
Fig. 1. Sketches showing interpolation/extrapolation between IB points and the grid points near the IB: (a) in Saiki and Biringen's scheme [17] and the present scheme, (b) in Mohd-Yusof's [11] scheme.

on the boundary, and zero elsewhere, and $\mathbf{S}$ is the convection term defined as:

$$\mathbf{S} = (\mathbf{u} \cdot \nabla)\mathbf{u}. \tag{8}$$

In Eq. (7), $\mathbf{v}$ is the desired velocity on a layer of grid points immediately inside the IB named the internal layer on which the direct forcing is applied to. An external layer is defined as a layer of grid points immediately outside the IB. According to [11], if the IB surface is stationary, a tangentially opposite-direction flow-field to the external-layer flow-field is specified on the internal layer inside the IB surface. The forcing is thus determined by pairing the velocity at the internal point to the velocity at the external point with a weighted interpolation, to enforce the desired tangential velocity (zero in this case) on the boundary. Such a pair is illustrated in Fig. 1(b) between Point 1 and Point 2.

2.3. The current computational scheme

The direct-forcing IB method used in this paper follows the concept in [11]. The governing equations, Eqs. (1) and (2), are discretized using the first order time-marching, with a semi-implicit term for the diffusion terms and the second-order Adams–Bashforth for convection and central differencing for diffusion. The S&B interpolation/extrapolation scheme is then used to interpolate the direct force. This force is exerted back on the grid points inside the IB.

The procedure involves a two-step, predictor–corrector procedure. The velocity predictor equation is:

$$\mathbf{u}^* = \mathbf{u}^n + \delta t \left\{ -\left(\frac{3}{2}\mathbf{S}^n - \frac{1}{2}\mathbf{S}^{n-1}\right) - \nabla P^* + \frac{1}{2Re}\nabla^2(\mathbf{u}^n + \mathbf{u}^*) + \mathbf{f} \right\}, \tag{9}$$

where P^* is an estimation to the pressure determined by:

$$\nabla^2 P^* = -\nabla \cdot [(\mathbf{u}^n \cdot \nabla)\mathbf{u}^n - \mathbf{f}]. \tag{10}$$

Then, with the following correction step, the real time velocity and pressure are given by:

$$\mathbf{u}^{n+1} = \mathbf{u}^* - \nabla\phi \tag{11}$$

and

$$P^{n+1} = P^* + \phi, \tag{12}$$

where ϕ is the solution of the modified pressure Poisson equation (PPE):

$$\nabla^2\phi = \nabla\mathbf{u}^*. \tag{13}$$

The forcing term, $\mathbf{f}$, is designed to minimize the error at the boundary between the actual (computed) velocity at the new time and the desired (physical) velocity on the boundary surface. It is defined as

$$\mathbf{f} = \begin{cases} \mathbf{f}_G & \text{for the internal-layer grid points,} \\ 0 & \text{elsewhere,} \end{cases} \tag{14}$$

where

$$\mathbf{f}_{G(i,j)} = \frac{1}{\delta t}\frac{1}{N_b}\sum_{n=1}^{N_b} D_{i,j}(\mathbf{x}_s)[\mathbf{V} - \mathbf{U}(\mathbf{x}_s)] + \left(\frac{3}{2}\mathbf{S}^n - \frac{1}{2}\mathbf{S}^{n-1}\right)_{i,j} - \frac{1}{Re}(\nabla^2\mathbf{u}^n)_{i,j} + \nabla P_{i,j}, \tag{15}$$

where N_b is the number of IB points affecting the current grid point at (i,j), $\mathbf{V}$ is the desired boundary velocity, and $\mathbf{U}(\mathbf{x}_s)$ is the computed boundary velocity. Since the IB points do not necessarily coincide with the grid points, the computed boundary velocity is first interpolated from the grid points to the boundary points using Eq. (5). Then in Eq. (15), the difference between the desired boundary velocity and the computed boundary velocity, $\mathbf{V} - \mathbf{U}(\mathbf{x}_s)$, is extrapolated back to the internal layer grid points using the same bilinear weighting functions to determine the direct-forcing term.

The computational scheme, including the interpolation/extrapolation procedure, is implemented on a staggered grid. Since the forcing is used to enforce the velocity on the boundary, the x-direction force is calculated on the u-grid and the y-direction force is calculated on the v-grid. Because the grid points involved in the interpolation/extrapolation procedure can be applied to either the u-grid or the v-grid, there would be no discrepancies between the staggered grid used in computing the governing equations and the grid used in the interpolation/extrapolation procedure. Mohd-Yusof's [11] original implementation was on a staggered grid too. The purpose of Fig. 1(a) and (b) is for illustration only, while the grid in Fig. 1(a) can also be considered either the u-grid or the v-grid for a staggered grid.

2.4. Discussion of the current method

The IB method presented here provides two major advantages over previous IB methods: it is more stable and less restrictive than the feedback-force methods because the direct forcing is used, which also removes the uncertainties related to the two negative coefficients in Eq. (4); in comparison to the previous second-order direct-forcing methods, the present scheme achieves comparable accuracy yet better conforms the geometry of the IB because the S&B interpolation/extrapolation method is used which allows more IB points to be used in the procedure without restrictions from the grid size near the IB.

2.4.1. Stability issue

The drawback of the feedback-force methods is primarily due to the restrictive stability requirement and the two constants involved. For the stability requirement for the feedback-force method in [4,17], it has been shown with the Adams–Bashforth method in [4] that

$$\Delta t < \frac{-\beta - \sqrt{\beta^2 - 2\alpha k}}{\alpha}, \tag{16}$$

where α and β are the two negative constants used in the feedback-force method, and k is a problem dependent constant of order one. In the flow-over-cylinder problem in S&B, the values of the coefficients are selected as $\alpha = -400{,}000$ and $\beta = -600$, resulting in a stability requirement of $\Delta t < 0.0012$.

For the direct-forcing methods, the calculation of the force does not influence the stability of the time integration, as stated in [2]. Therefore the stability requirement for direct-forcing methods using a two-dimensional fully explicit scheme with central differencing in space (FTCS) would be the same as that shown in [15]:

$$\delta t < \min \left[\frac{h^2 Re}{4}, \frac{2}{(u^2 + v^2)Re} \right], \tag{17}$$

where h is the grid size. The first restriction in Eq. (17) is for diffusion and the second restriction is for convection. Therefore, the stability requirement for the current scheme, that uses a semi-implicit scheme for the diffusion terms and the Adams–Bashforth for convection and central differencing for diffusion, is no more restrictive than this, because the semi-implicit scheme for diffusion should relax the first restriction and the Adams–Bashforth scheme for convection should relax the second restriction. For the low Reynolds number cases discussed and the grid sizes used in this paper, the time steps are in the range of 0.002875 to 0.05. In the implementation, we found that for the low Reynolds number case ($Re = 40$), the time step can be as large as two times of what is restricted by this requirement. This shows the time steps in the direct-forcing methods can be much bigger than those in the feedback-force methods. Another evidence that shows feedback-force methods generally have more restrictive stability requirement is in [8], where a stability condition of

$$\Delta t \sim C \sqrt{h/\kappa} \tag{18}$$

is presented, where κ is a stiffness constant in the order of 10^4 to 10^5.

2.4.2. IB interpolation/extrapolation

In Mohd-Yusof's method [11], if the numbers of grid points on both of the internal and external layers are exactly the same, pairs of boundary points can easily be formed. Assuming that the external-layer velocity is the corrected one from the previous time-step computation, the velocity of the external layer along with the desired IB velocity on the IB point can be used to determine the internal-layer velocity $\mathbf{v}$ in Eq. (7). The weight of each of the velocity is proportional to the ratios of the distances from the points of each side to the IB surface. Points 1 and 2 in Fig. 1(b) are a perfect pair which can fulfill this type of interpolation. This interpolation method works well in some applications, but it also has some drawbacks. One is that only are tangential velocities exerted as forcing to the internal layer. It was claimed in [11] that including the normal velocities led to a large accumulation of mass at the IB or significant flow-through at the boundary due to the absence of boundary surface points. The other is that in practice, some IB geometries cause the number of external points unequal to the number of internal points. Then the selection of the two points representing each pair is sometimes arbitrary. In Fig. 1(b), the internal point, Point 3, could be paired with either Point 4, Point 5, or even Point 6. Therefore extra efforts are needed to define the internal and external pairs of points. Finally, since the IB points do not exactly coincide with the grid points, the smoothness and accuracy of the IB would depend on the grid size near the boundary in the interpolation used in [11]. Because of the above mentioned drawbacks, a higher-order interpolation is therefore needed for accurate IB representation if the direct-forcing IB method is to be used.

It should also be pointed out that there is a difference between the direct-forcing IB method represented in Eq. (15) and the one by Mohd-Yusof [11] represented in Eq. (7). In Eq. (15), the physical velocity on the IB, $\mathbf{V}$, is used, while in Eq. (7), the interpolated internal-layer velocity, $\mathbf{v}$, is used. Particularly in [11], only the tangential component of the interpolated velocity was used for specifying the force, while in Eq. (15) both of the tangential and the normal velocity components are included.

On the other hand, S&B used a bilinear interpolation/extrapolation scheme when mapping the grid-point values to the IB values. When this scheme is used in this paper to interpolate/extrapolate between the grid points and the IB points in the direct-forcing method, the IB velocity at each IB point (Point A in Fig. 1(a)) is determined by velocities of those closest grid points (Points 1–4) using a weighting function. Each of these grid points then receives the average forcing of all the IB points close to them. Subsequently, each grid point in the vicinity of the IB receives inputs from multiple IB points. This procedure is also easy in coding. In addition, because the interpolation/extrapolation procedure uses the physical velocity on the IB, both the tangential and normal velocity effects are automatically included with this type of interpolation/extrapolation

(while in Mohd-Yusof's scheme [11] only the tangential velocity was used and specified on the internal layer for forcing). The forcing has a contribution from the difference between the desired IB velocities and the actually calculated IB velocities mapped to the internal layer, in order to correct the IB velocities to the desired velocities. This modification is able to improve the accuracy in the region near the IB surface.

2.4.3. Resolution of IB points

The number of IB points, denoted as N_b in Eq. (15), has the same meaning as the N_b in S&B. In Fadlun et al.'s [2] direct-forcing interpolation, the IB resolution is determined by the grid resolution, because only the IB points that intercept the Cartesian grid lines are interpolated, as shown in their Fig. 2. Therefore the resolution of the IB points are limited by the resolution of the grid lines near the boundary since only the intercepted points are considered IB points. That is, the interpolation cannot be mapped to resolve the points smaller than the grid size. In the interpolation procedure used in the current method to get the boundary velocities in Eq. (5), the points selected on the boundary (with locations denoted as $\mathbf{x}_s$) do not need to coincide with the grid points or intercepted points, as shown in Fig. 1(a). Therefore in order to increase the resolution just on the boundary, many more points (in fact arbitrary number of points) in between the intercepted points can be used to represent the IB points to be used to obtain the velocity values, $\mathbf{U}(\mathbf{x}_s)$ in Eq. (5), and to be used later for extrapolating forcing back to the grid points in Eq. (15). In this sense, the number of boundary points used in Eq. (15), N_b, can be independently increased without being restricted to the resolution of the computational grid for the flow. For example, in Fig. 1(a), we can add another boundary point, Point B, other than Point A but still surrounded by the same group of grid points 1, 2, 3, and 4. The difference in the velocity values between Point A and Point B is due to the difference in the weighting functions. By defining different weighting functions for different IB points to be used with the same group of grid points, many different boundary points can be added. With this procedure, the influence of the IB surface can be better represented because the smoothness and accuracy of the IB surface can be independent of the grid size. As shown by using Fig. 1(a) as well as Fig. 4 in S&B [17], a very smooth representation of the boundary curve can be achieved. There is no limit on how many points can be distributed on the boundary. Of course, the increase of accuracy can reach a limit by just adding boundary points without increasing computational grid resolution. The flow information used for interpolation/extrapolation is still limited by the close neighbor points within one grid cell (which is why the S&B interpolation is still considered first order), and thus the overall accuracy is still
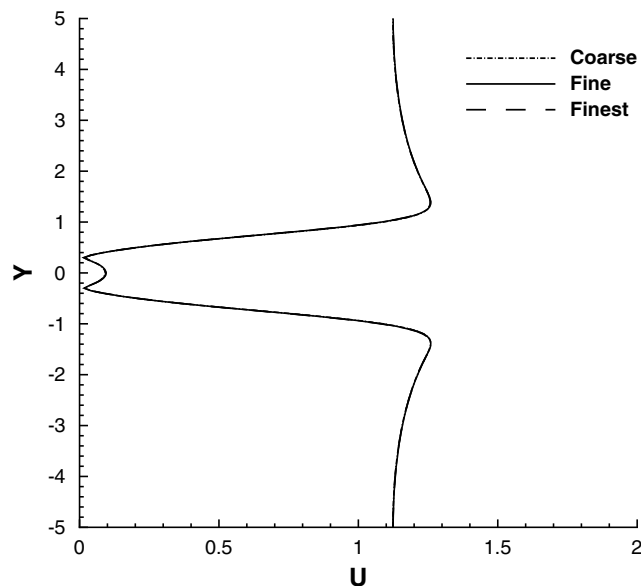

Fig. 2. Comparison of velocity-magnitude profiles at $x = 1$, among coarse, fine and finest grid results, with $Re = 40$ for a stationary cylinder.

limited by the Cartesian grid resolution. However, within such a limit, the local accuracy on the boundary can be improved by using more IB points to represent the boundary. The advantage of having finer resolution for the boundary points will be discussed further with some numerical results of flow over a cylinder in the next section, where a substantial evidence of an L_2-norm plot related to the resolution of IB points will be presented.

2.4.4. Internal layer for specifying forcing

In the original S&B scheme, the interpolation/extrapolation method did not need to define either an internal or an external layer, and thus the coding was simple. However, this simplicity also caused inaccuracy. In [17], it was stated that this approach was successful in capturing large scale features, but not so accurate at the region immediately near the IB. The reason is if the IB forces are extrapolated back to the grid points on both the internal and external layers, as the result of numerically applying forcing on these grids, an equivalence of a "zig-zag" boundary is created. Therefore the boundary curve is diffused. An extreme case is when two grid points, one internal and the other external, locate at the same normal distance from each side of the surface curve. Then exactly the same force would be exerted on these two points to enforce zero velocity at both of the grid points. This leads to a situation that both of them can be considered boundary points, resulting in a boundary with the thickness at this location equivalent to the distance between the two points. Consequently, the deterioration of the smoothness and accuracy of a well-defined IB is likely responsible for the inaccuracy at the region immediate to the IB. The errors caused by extrapolations to both external and internal layers can be singled out when we compare the results between forcing on the internal layer only and forcing on both sides in the flow over cylinder case in the next section.

In the current scheme, the direct forcing is consistently applied to the internal layer (the first grid layer interior to the solid body) to avoid numerically thickening the boundary curve. From another point of view, the external layer is part of the flow-field and should not be "hardened" to be part of the boundary. An internal layer is thus defined for applying the IB forcing. Note that the grid point (i,j) in Eq. (15) is on the internal layer only. The weighting functions in the expression are used to extrapolate the force on the IB points back to the grid points on the internal layer to prescribe direct forcing there. If we use Fig. 1(a) to explain the different ways of mapping the forcing back to the grid points, the method of S&B maps the forcing back to all the points from 1 to 10, while the current method only maps to points 2 and 7–10.

2.4.5. Treatment of the interior to the body

In Fadlun et al. [2], three possible ways of treatment for the flow interior to the body are tested. The first is to apply the forcing at every point inside the body, as suggested by S&B. The second is to leave the interior of the body free to develop a flow without imposing anything. The third is to reverse the velocity at the first point inside the body in such a way that results in the desired velocity on the boundary. For the finite-difference direct-forcing method used in their work, the external flow remains the same with the three different ways of internal body treatment, although the flow inside the body is different resulting from different internal treatment.

The internal treatment of our method is the same as the second way, i.e., the flow interior to the body is free to develop. The indifference of the external flow to the internal treatment in finite-difference methods is due to the smaller width of stencil in the matrices resulting from finite-difference methods, in comparison to those from spectral methods, as indicated in Fadlun et al. and S&B. In spectral methods, the misbehavior near the boundary and interior to the body can deteriorate the solution in the external flow because of the global nature of spectral methods. To test the partition effect (i.e., different internal treatment resulting in the same external flow) of IB in the finite-difference scheme used in this paper, we force the internal flow velocity to be zero inside the cylinder, which is physical but causes an abrupt change in the internal flow region. As expected, the external flow and even the surface variables such as C_p only show very minor changes. Therefore, when the IB is properly represented, it can accommodate different types of internal treatment without influencing the external solution. Obviously, for the current scheme letting flow inside the body develop freely is simple in coding and low in computational cost if the external flow is not influenced. While S&B found in some cases that by only imposing the force at the boundary their method would converge to the incorrect solution, as discussed previously, the incorrect solution in S&B's case can possibly be attributed to specifying forces on both sides of the IB.

3. Validation cases

3.1. Flow over a cylinder

The Reynolds number range for the validation cases of a stationary cylinder is from 40 to 200. One case of an oscillating cylinder has been run with $Re = 200$. The numerical model for the cylinder cases is two-dimensional and time-dependent, and is nondimensionalized by the diameter of the cylinder D and the free-stream velocity U_o. The computation is performed on a staggered grid mesh. The domain size is 26×10. The center of the cylinder is located at 6 from the inlet which is sufficient to avoid inlet boundary effects [15].

The time-marching scheme is a two-step predictor–corrector procedure, as explained in Section 2.3. The convection terms are discretized using the second-order Adams–Bashforth method, and the diffusion terms are discretized using the second-order central differencing. Via suggestions in [17], the normal direction diffusion terms are advanced implicitly using the Crank–Nicolson scheme. The two Poisson equations at each time step (one for P^* and one for ϕ) are solved using the Fishpack subroutines [19].

For the boundary conditions, at the inlet, $u = 1$, $v = 0$ and $\partial P/\partial x = 0$ are prescribed. On the top and bottom boundaries, $\partial u/\partial y = 0$, $v = 0$ and $\partial P/\partial y = 0$ are imposed. At the outlet, the two velocity components are assumed to have zero normal gradients, and $P = 0$. The boundary conditions for ϕ are zero normal gradients at the inlet, the top and the bottom boundaries, obtained from Eq. (11) with the fact that $\mathbf{u}^{n+1} = \mathbf{u}^*$ on these three boundaries. The value of ϕ is set equal to zero at the outlet. The current pressure boundary conditions at the inlet and outlet boundaries are imposed to be consistent with the equations for the velocities due to the staggered grid arrangement [15]. While the $P = 0$ boundary condition has to be specified either at the inlet or the outlet boundary, inconsistency would occur if $P = 0$ was specified at the inlet. That is because on the staggered grid, the grid points for $u(0,j)$ are located on the inlet boundary, while those for $P(0,j)$ are half grid-point outside and those for $P(1,j)$ are half grid-point inside the inlet boundary. If $P = 0$ is set at the inlet boundary, at each time step, $P^*(0,j) + P^*(1,j) = 0$. Because $u(0,j) = 1$, from Eq. (11), $\partial\phi/\partial x = 0$ at the inlet. Then with Eq. (12), $P^{n+1}(0,j) + P^{n+1}(1,j) = P^*(0,j) + P^*(1,j) + 2\phi$ is nonzero in general, which causes inconsistency to the condition that $P = 0$ on the inlet. Thus the current pressure boundary conditions are appropriate on a staggered grid.

The grid-size independence test has been performed for the stationary cylinder case to determine the resolution. There are three levels of grid sizes, namely coarse, fine and finest. The grid size of each level is 0.05, 0.025 and 0.0125, respectively. Fig. 2 is the comparison of velocity-magnitude profiles at $x = 1$ from the center of cylinder, with $Re = 40$. Fig. 3 is the comparison of the top half surface C_p (defined as $C_p = 2(P - P_{\mathrm{ref}})/U_o^2$) for the same case. From Fig. 2 it can be clearly seen that the results from all three grid-size levels are identical in the near wake region. While the near wake region usually imposes more restrictive resolution requirements, Fig. 2 shows that the lowest level grid size is sufficient for the study of the entire wake region. On the other hand, Fig. 3 represents the accuracy on the immersed boundary itself. The fine- and finest-grid results are closer to each other than the coarse grid result. This means the fine grid used in the computation is sufficient for the detailed study of the flow-field close to the cylinder. Therefore for the results shown in this paper, the comparisons of the C_p values on the cylinder surface are using results from the fine-grid simulation, and the other values are all computed from the coarse grid simulations for the purpose of saving computational costs. The dimensionless time step used in the computation is 0.004883 for both of the coarse and fine grids, which satisfies the stability condition imposed by Eq. (17) for all of the Reynolds-number ranges.

In order to provide the evidence to the arguments made in *Resolution of IB points* in Section 2.4 regarding the IB points resolution and to show the rationale of how many IB points to select, we investigate the behavior of a local variable and an external variable, the C_p on a cylinder surface and the x-direction velocity of all the points along the x-axis, when we change the density of number of IB points. We want to test how the relative error norms of these two variables change when the number of boundary points per Cartesian meshwidth changes. Fig. 4 shows the L_2-norms of C_p and u-velocity along the x-axis for flow over a stationary cylinder at $Re = 40$, when the number of IB points is selected to be 60, 120, 240, 480, 960, 1920, 3840, and 7680 with the Cartesian grid spacing of $\Delta x = \Delta y = 0.025$. The finest IB-point density case with 7680 IB points is the base for estimating the L_2-norms. We notice that with the current grid size used in the computation of $\Delta x = \Delta y = 0.025$, the number of intercepted grid on the Cartesian grids near the boundary is approximately 160.
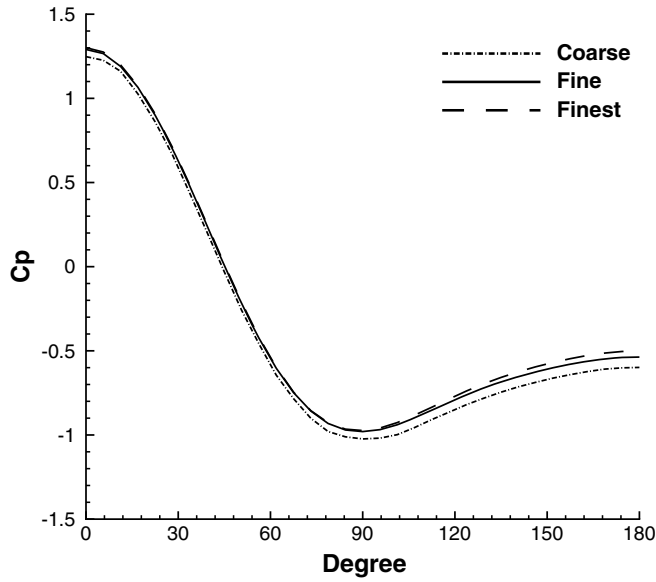
Fig. 3. Comparison of the top cylinder-surface C_p among coarse, fine and finest grid results, with $Re = 40$ for a stationary cylinder.
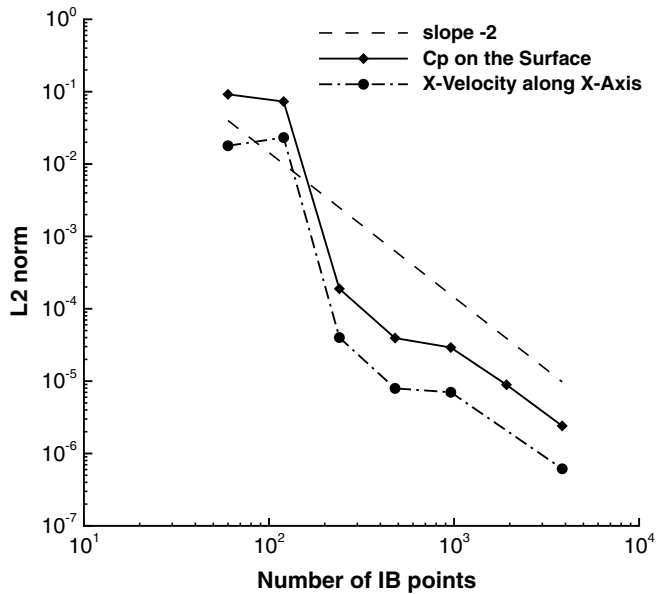

Fig. 4. The L_2 norms versus the number of IB points, of the surface C_p and the x-direction velocity component at all of the points along the x-axis through the center of the cylinder.

These cases cover the range of the intercepting IB points per Cartesian grid approximately from 0.3 to 48. It can be seen that the L_2-curves fluctuate around a "−2" slope, and stagnancy of accuracy improvement shows at certain stages of IB number increase. This figure can change if the Cartesian grid resolution is changed. The change would show steeper slope at the part of smaller number of IB points with higher grid resolution. In Fig. 5, the C_p distribution for the same case is plotted, which shows that after 240 IB points, the improvement of the accuracy cannot be discerned by eyes. While the number of Cartesian grids near the boundary is approximately 160, any number of IB points that is not significantly greater than 160 causes information "leak" on the IB. Therefore the cases with 60 and 120 IB points lead to incorrect results as shown in
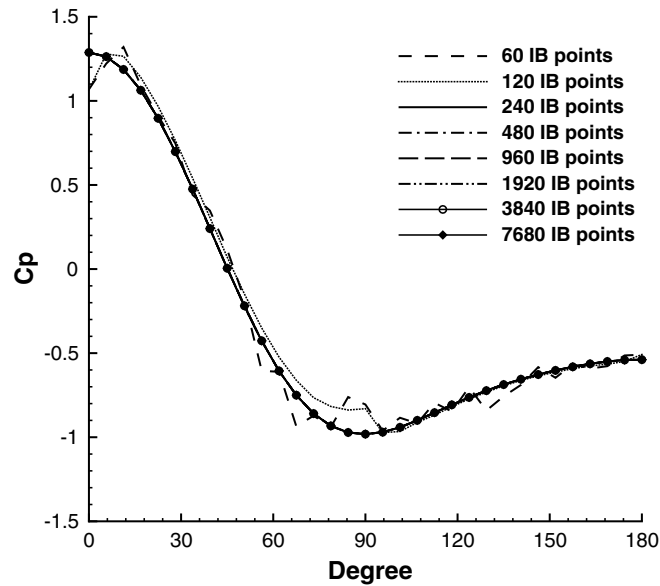
Fig. 5. The surface C_p distributions with different numbers of IB points.

Fig. 5, because the densities of IB points in these two cases are less than 1 per Cartesian grid. When the number of IB points is 240, there are about 1.5 IB points per Cartesian grid. When 240 or more IB points are used, the solution becomes good and converges at a second-order rate. Although the boundary resolution of 240 IB points can be acceptable, it is just at the margin of having an insufficient boundary resolution according to Fig. 4. In the computational results presented in this paper, the number of IB points of 960 is thus selected to leave enough "cushion" to avoid incidentally reaching a bad boundary resolution. Therefore the capability of arbitrary increasing the number of IB points for interpolation does have advantage over a scheme that only allows the intercepted IB points to be used.

We notice that in S&B the number of IB points on the cylinder is 1441 with their near boundary grids of $\Delta x = \Delta y = 0.0375$. Although the detailed reasoning of selecting this number is not provided in S&B, according to Fig. 4 there is a sufficient resolution in their IB points. We also notice that the computational cost of having a lot of IB points in S&B could be much more than that in the current direct-forcing method, because there is the integration with time on every IB point in the feedback force method in S&B.

On a certain Cartesian grid with which a reasonable resolution of solution is obtained according to the overall Cartesian grid resolution check such as using Fig. 6 (to be discussed later), Figs. 4 and 5 show that by increasing the density of IB points, the solution converges to the "best value" that can be achieved using this particular Cartesian mesh, but not necessarily the "true value" in the absolute sense. This "best value" itself is, of course, limited by the overall Cartesian grid resolution. It should be noted that Fig. 4 provides only one way to look into the influence of the IB point density, and is by no means trying to totally resolve the issue of convergence of the IB-like method. The overall convergence issue involving interface jumps such as those near the IB is investigated by Tornberg and Engquist [20].

In order to determine the approximate order of accuracy of the current direct-forcing method, we plotted an L_2-norm of error in Fig. 6 to indicate the accuracy of the computational scheme. The variable of which we selected to calculated the norm is the velocity component at the flow direction (x-direction). The values are for all the points along the x-axis (through the center of the cylinder), except inside the cylinder where there is physically no flow. We use different grids ranging from 130×50 to 2080×800, with the grid sizes of 0.2, 0.1, 0.05, 0.025 and 0.0125. Regarding the solution on the finest grid as "exact" (as done in [2]), the errors of the solution are computed on the coarser grids. When changing the grid resolution, the norm shows a "-2" slope in the log–log plot of the norm versus the grid number. This means that the overall computational accuracy is second order in space. This is not surprising because the computational scheme used in this paper
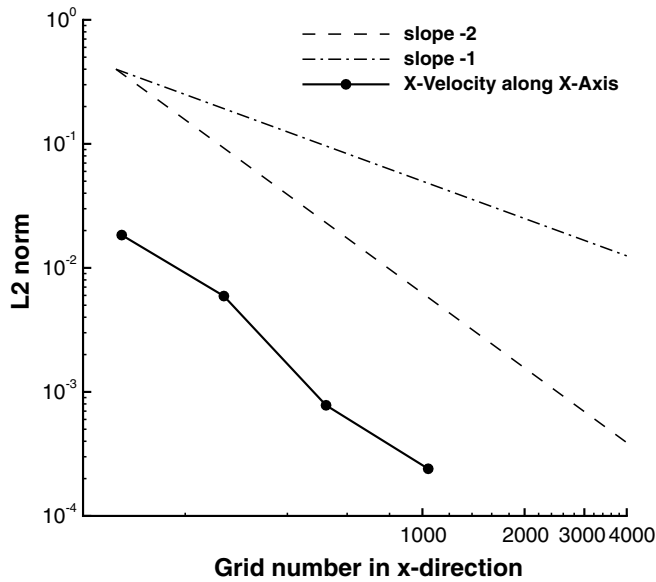
Fig. 6. The L_2 norm versus the grid number, for the x-direction velocity component at all of the points along the x-axis through the center of the cylinder.

is second-order accurate in space. In Fadlun et al.'s paper [2], a second-order accuracy was also achieved. As pointed out in their paper, their direct boundary forcing was a result of a linear interpolation of the velocity near the boundary. They stated that the S&B scheme was first order and therefore only the first order accuracy could be achieved. In the present scheme, although the spatial second-order accurate scheme and the second-order bilinear interpolation are used, the location for extrapolating the boundary force back to the Cartesian grid is still shifted on the first-order of one-grid-cell space, similar to that pointed out by Saiki and Biringen [17] and by Fadlun et al. [2]. However, we have shown in Fig. 6 that by using the S&B interpolation (which is a second-order bilinear interpolation), a second-order spatial accuracy is still achieved. The possible reason is that a relatively large number of IB points are used for the interpolation/extrapolation procedure in the current scheme because the IB points can be refined independently to the computational grid points. Therefore, the accuracy in the region near the boundary can be improved to remedy the first-order effect, without using higher-order scheme, or arranging complicated grids near the boundary as embedded grids (e.g., those mentioned in [2]), ghost cells [21], or the Lagrangian points [19].

Low Reynolds number flow over a stationary cylinder is first used as a validation for the modified IB interpolation method. The validation is done by investigating the surface-pressure distribution at the cylinder solid surface boundary, which can be very sensitive to the implementation of the interpolation/extrapolation procedure near the IB. According to Zdravkovich [23], at the low Reynolds-number range of $Re \leqslant 50$, a pair of attached, steady and symmetric bubbles exist downstream of the cylinder. Since no vortex shedding has been formed, the C_p on the cylinder surface is steady. Fig. 7 shows the C_p on the cylinder surface at $Re = 40$ comparing the result of the current method to those of Tseng and Ferziger's direct-forcing, second-order, quadratic-polynomial-reconstruction, ghost-cell scheme [21], Silva et al.'s direct-forcing, 2nd order Lagrangian-points scheme [19], along with the experimental data from [6]. The plots show that the current scheme is very close to Tseng and Ferziger's as well as the experimental data, and better than Silva et al.'s second-order scheme. This means again that the current interpolation/extrapolation procedure can achieve as a good or better accuracy near the boundary in comparison to some of the complicated boundary interpolation schemes mentioned previously.

Another comparison has been made using three different IB methods: the first using the current method that implements the direct forcing in combination with the modified S&B interpolation/extrapolation, the second using the original S&B [17] IB method based on Goldstein's [4] feedback-force IB method with forcing on
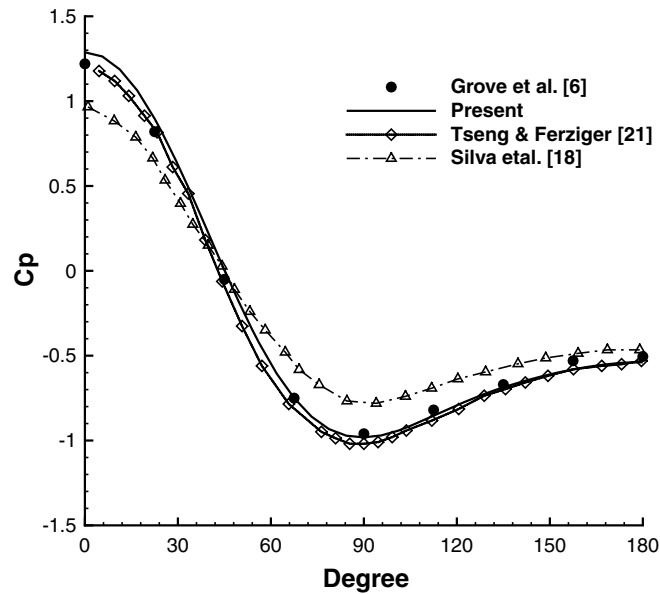
Fig. 7. C_p on the top surface of the stationary cylinder, $Re = 40$. Compare the current result to the results of the second-order direct-forcing IB methods in [21,18] and to Grove et al.'s [6] experiment.

both the external and internal layers, and the third using the S&B feedback-force method with forcing on the internal layer only. The results of the S&B method are from our own implementation exactly following the steps in their paper. The two empirical constants in the feedback-force method are $\alpha = -400,000$, and $\beta = -600$. All of the parameters of the two feedback-force schemes are the same as the current direct-forcing method, except that the time step is four times smaller due to the restriction of the feedback-force method. Fig. 8 shows that the two curves from the present IB method and from the feedback-force method with forcing on the internal layer match very well, while the result from forcing on both the external and internal layers shows errors. This tends to agree with the fact that both direct-forcing and feedback-force methods produce essentially identical results, if the forcing in both cases is properly specified. Forcing on both sides of the IB
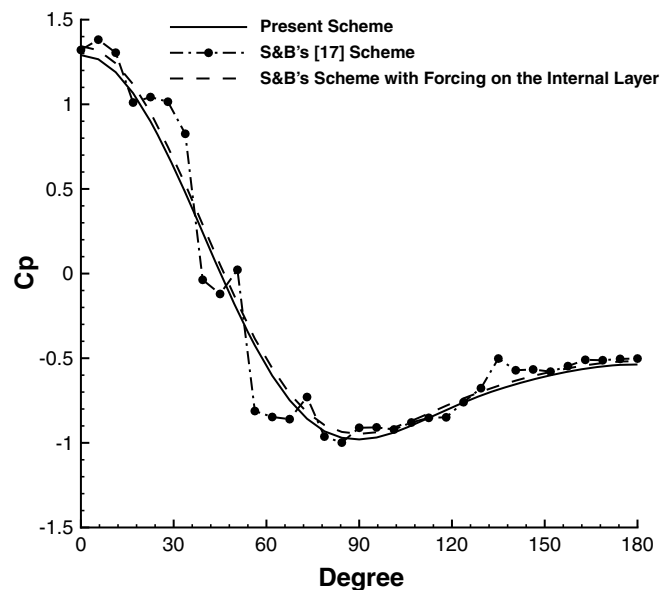

Fig. 8. C_p on the top surface of the stationary cylinder, $Re = 40$. Compare the current result to the results of Saiki and Biringen's [17] original IB method and Saiki and Biringen's method but with forcing on the internal layer only.

creates errors that lead to zig-zag C_p distributions and deteriorate the smoothness of a well-defined IB. A more detailed discussion about the difference in the way of mapping the forcing back to the grid points, between the current method and that used in the S&B, has been presented in the subsection of *Internal layer for specifying forcing* in Section 2.4. This also shows that the advantage of the current scheme over that of S&B is the same as a direct-forcing scheme over a feedback-force scheme, that is, to use the direct forcing so that larger time steps can be used.

At larger Reynolds numbers ($Re \geqslant 50$), there is an unsteady wake, i.e., the von Karman vortex street, shed from the cylinder surface. The Strouhal number of the vortex shedding frequency, defined as $St = fD/U_o$, is often used as a criterion for validating computation since it varies with the Reynolds number. Fig. 9 is a comparison of St versus Re to the previous numerical results by Ravoux et al. [15] (a direct-forcing IB scheme), Zhang et al. [24] (a curvilinear orthogonal grid scheme), Lai and Peskin [8] (a feedback-force IB method) and Silva et al. [18] (a direct-forcing IB method), and experimental data by Williamson (as reported in [9]) and Konig et al. [7]. The present computation was run for 60 periods and the result was based on the data between 28 and 60 periods so that the accuracy of the St is 0.00625. Fig. 9 shows that the two experimental data sets are very close, with Williamson's data reaching to a larger Reynolds number range. The computational results of the current method, [15,24] tend to over-predict the St number, and the computational results of [8,18] tend to under-predict the St number. The present computational result is close to that of [15], with a bit less over-prediction in comparison to the experimental data.

Cases of high Reynolds numbers at 400, 500, and 550 are also included to compare with Roshko's [16] experimental data. Saiki and Biringen [17] state that their scheme converges to an incorrect solution for $Re = 550$ (with no results shown) when they allow the velocity field to be nonzero within the body. In our present scheme, spatial oscillations occur near the IB. However, these oscillations basically remain the same under the three types of interior treatment discussed in Section 2.4 under *Treatment of the interior to the body*. As discussed in that section, the same uninfluenced external flow was also observed in Fadlun et al.'s [2], which they attributed to the fact that the direct-forcing was used in their IB method, instead of the feedback force. This partition effect of IB with direct forcing is thus confirmed in our results. We then opt to use an upwind spatial differencing in a small region in the vicinity of the IB to remove the oscillations. Fig. 10 is to compare the results using the present scheme and the S&B scheme [17] that we implemented for Reynolds numbers of 400, 500, and 550, along with Roshko's experimental data [16]. It shows that with the S&B scheme, the results do not follow the trend observed from the experiment, and the Strouhal number increases strongly with the
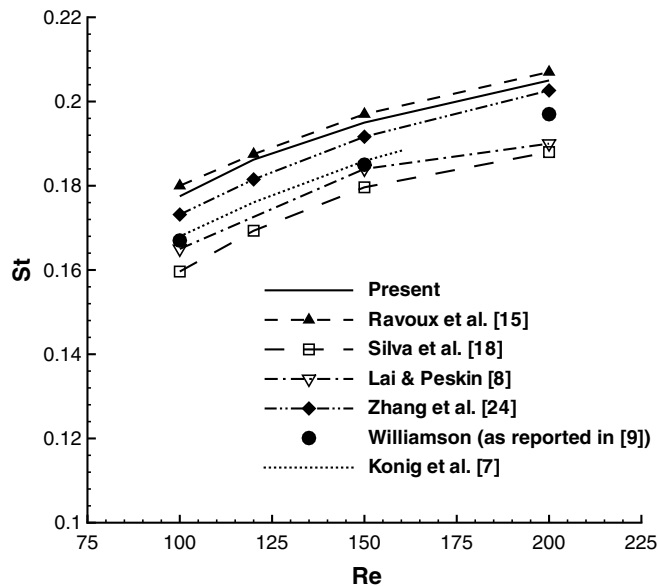

Fig. 9. Plot of Strouhal number vs. Reynolds number from 100 to 200 for flow over a stationary cylinder, with comparison to previous numerical and experimental results.
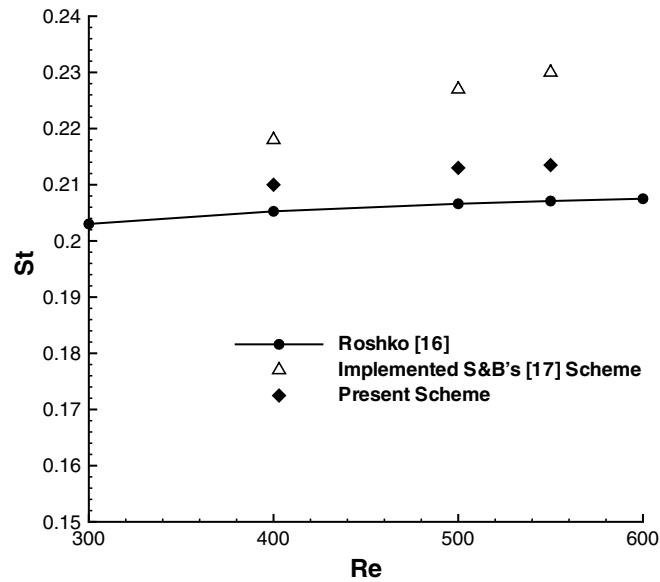
Fig. 10. Plot of Strouhal number vs. Reynolds number from 400–550 for flow over a stationary cylinder, with comparison to the results from implemented S&B scheme [17] and experimental results in [16].

increase of Reynolds number. On the other hand, the results from the present scheme follow the trend of the measured data. These results justify the accuracy of the present scheme in high Reynolds number cases.

Oscillating cylinder results are compared with experimental data by Griffin's hotwire measurement [5], at a Reynolds number of 200. The oscillation in the cross-flow direction has the dimensionless displacement of

$$d_y = 0.15 \sin(2\pi t * St). \tag{19}$$

The oscillation St number in the measurement was selected at the vortex shedding frequency and was close to 0.2 for the case discussed here. Fig. 11 is the vorticity (of the component perpendicular to the paper surface) contours after 40 oscillation periods. After about 15 periods, the flow is very close to periodic. In this figure, the von Karman vortex street is fully developed and can be clearly observed. Notice that there is flow both inside and outside of the cylinder, since the IB method computes the flow on the entire Cartesian grid without regard to the location of the physical boundary of the body. For the purpose of comparison, the ratio between
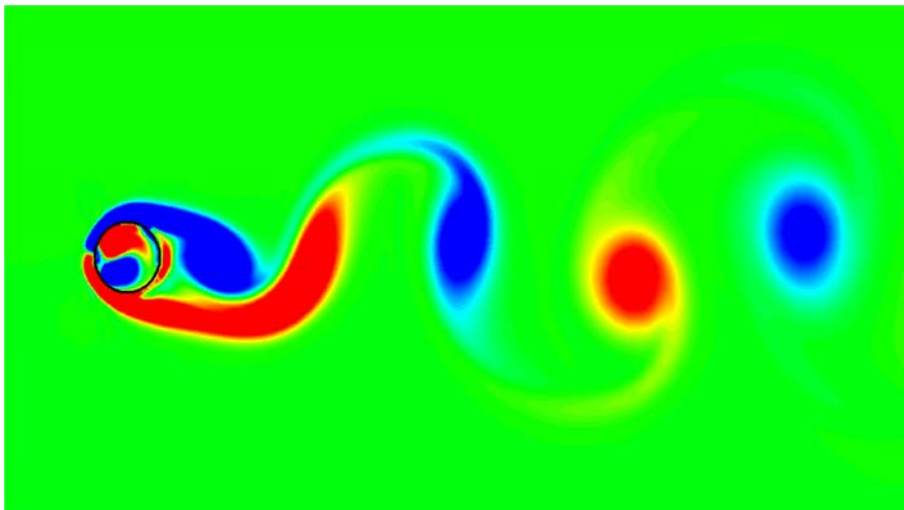

Fig. 11. Vorticity contours for the oscillating cylinder case after 40 oscillating periods, with $Re = 200$.

the root-mean-square (RMS) velocity-magnitude fluctuations and the mean free-stream velocity magnitude is selected as the representative of the flow fluctuation quantity. Fig. 12 is the comparison of the RMS velocity-magnitude fluctuation profiles with Griffin's [5] experimental results, at two different streamwise locations in the wake region: $x = 2.5$ and $x = 5.4$. The coordinate origin is the averaged center of the oscillating cylinder. The major features of the profiles, i.e., the downstream decaying and the spreading of the RMS velocity-magnitude fluctuations, have been captured with very good agreement. In Fig. 13, changes of the maximum RMS velocity-magnitude fluctuations versus the downstream (x) locations in the wake region are plotted along with Griffin's experimental result. Finally, Fig. 14 is the RMS velocity-magnitude fluctuations on the wake axis ($y = 0$) versus the downstream locations. Griffin used the downstream location of the peak in Fig. 14 to determine the end of the vortex formation region, and Fig. 14 shows that this location can be determined by the computation with very high accuracy. The above comparisons have demonstrated that good agreements have
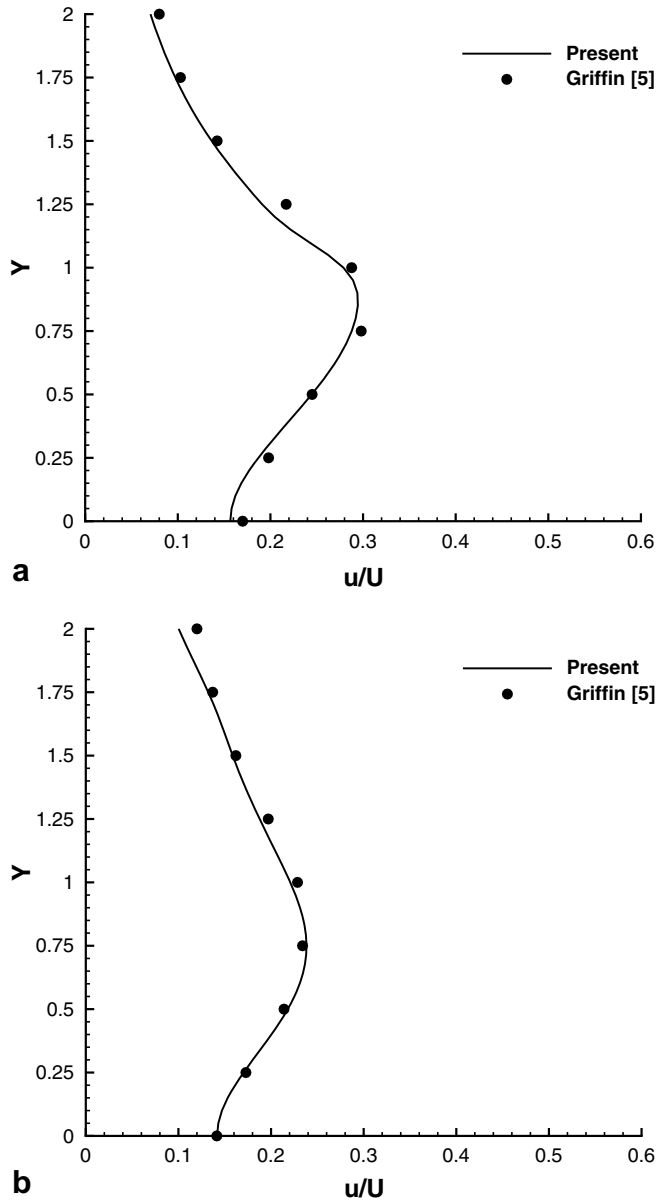

Fig. 12. Comparison of RMS velocity-magnitude fluctuation profiles for the oscillating cylinder case at $Re = 200$, with results from the present IB method and Griffin's [5] experiment at two different streamwise locations, (a) $x = 2.5$, (b) $x = 5.4$.
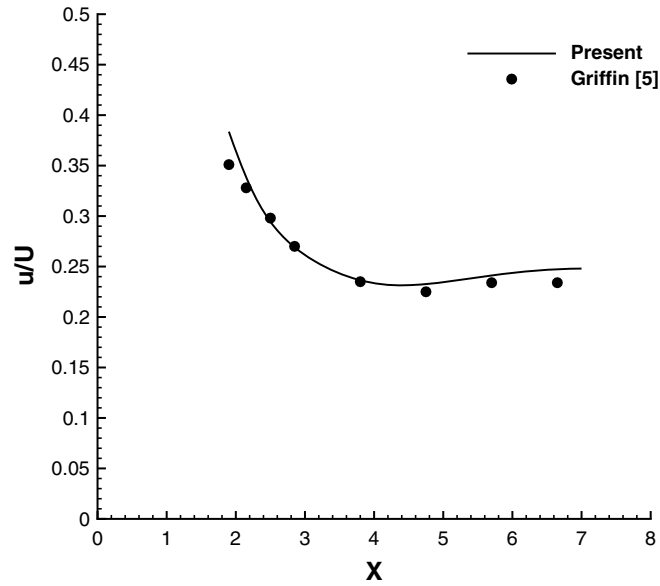
Fig. 13. Comparison of maximum RMS velocity-magnitude fluctuation vs. streamwise location x, with results from the present IB method and Griffin's [5] experiment, for the oscillating cylinder case, $Re = 200$.
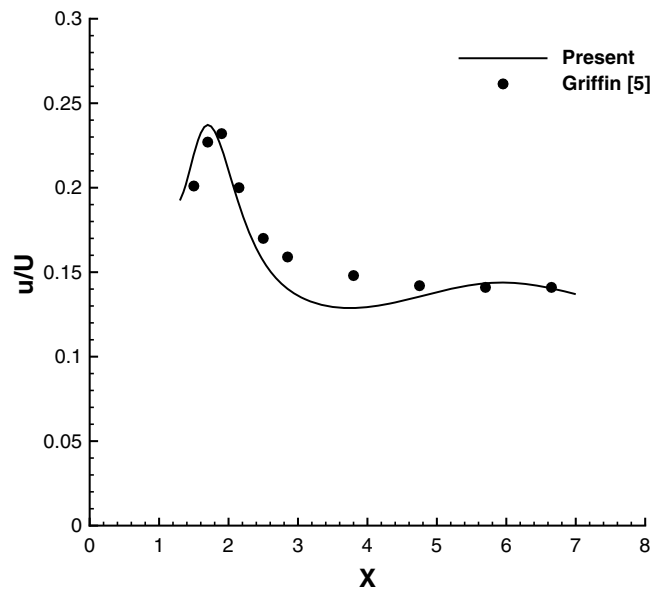

Fig. 14. Comparison of RMS velocity-magnitude fluctuations at wake axis ($y = 0$) vs. streamwise location x, with results from the present IB method and Griffin's [5] experiment, for the oscillating cylinder case, $Re = 200$.

been achieved in all of the unsteady features in comparison with Griffin's experimental results as evident in Figs. 12–14. These unsteady flow features usually pose challenges for computational simulations to capture.

3.2. Flow over a sphere

In order to compare a three-dimensional case, flow over a stationary sphere has been simulated using the current method. The domain size is $14 \times 3.2 \times 3.2$ (14 in the incoming flow direction), the same as in [11]. The sphere is centered at $(4, 1.6, 1.6)$. A uniform Cartesian grid is used with the size of $\Delta x = \Delta y = \Delta z = 0.05$,

and the size of the time step is 0.0125. The number of IB points on the sphere is 11,240, evenly distributed on the sphere surface. The Reynolds number is from 30 to 100 so that the axisymmetry of the flow is guaranteed [10]. In this Reynolds number range the axial length of the separation bubble, defined as the distance between the rear end of the sphere and the first point on the axis where the *x*-direction velocity component $u = 0$, grows linearly with the Reynolds number [1]. Fig. 15 is the length of the separation bubble versus the Reynolds number, in comparison between the present results with those of Batchelor [1], Fadlun et al. [2] (from direct-forcing IB computation) and Fornberg [3] (from boundary-fitted mesh computation). A very good agreement has been achieved among the four sets of data. Fig. 16 is the C_p distribution on the sphere surface at $Re = 100$. The comparisons of the present result to those of Fadlun et al. [2] and Fornberg [3] are again in good agreement. Figs. 15
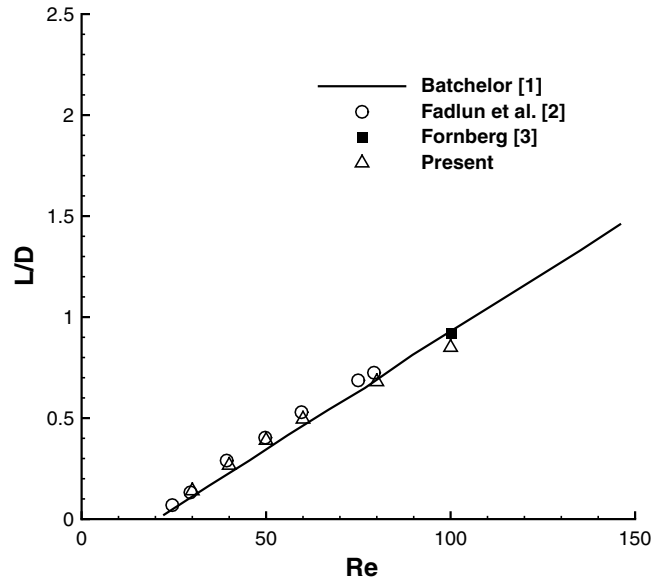

Fig. 15. Comparisons of the length of the separation bubble versus *Re* for flow over a sphere between the present results and the results in [1–3].
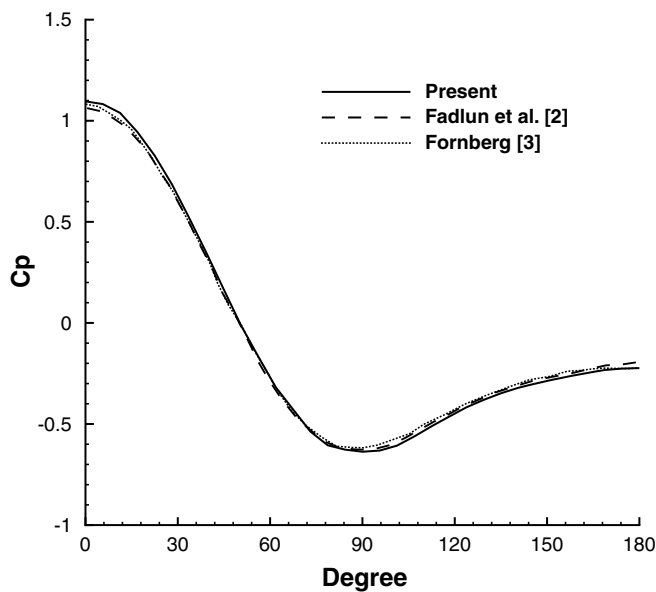

Fig. 16. Comparisons of the C_p distributions on a sphere between the present results and the results in [2,3] at $Re = 100$.

and 16 show that a three-dimensional implementation of the current method is able to obtain credible computational results in comparison to the other direct-forcing IB methods [2] and none-IB methods [3].

4. Conclusions

The modified IB method developed in this paper is based on direct forcing in combination with an improved interpolation/extrapolation method. The modifications have relaxed the stability requirement comparing to feedback-force methods, improved simplicity of implementation, and achieved the same accuracy comparing with other high-order direct-forcing methods. By comparing with the numerical and experimental results in the literature, the validation cases have shown that a second-order spatial accuracy has been achieved in computing both of the steady and unsteady features of flow around a circular cylinder. In particular, the fact that the present IB method captures unsteady flow features accurately provides a strong evidence of the capability of this new method. The three-dimensional cases of flow over a sphere also show good agreements with the literature data.

Acknowledgement

References

[1] G.K. Batchelor, An Introduction to Fluid Mechanics, Cambridge University Press, Cambridge, UK, 1967.
[2] E.A. Fadlun, R. Verzicco, P. Orlandi, J. Mohd-Yusof, Combined immersed-boundary finite-difference methods for three dimensional complex flow simulations, J. Comp. Phys. 161 (2000) 35–60.
[3] B. Fornberg, Steady viscous flow past a sphere at high Reynolds number, J. Fluid Mech. 190 (1988) 471–489.
[4] D. Goldstein, R. Handler, L. Sirovich, Modeling a no-slip flow boundary with an external force field, J. Comp. Phys. 105 (1993) 354–366.
[5] O.M. Griffin, The unsteady wake of an oscillating cylinder at low reynolds number, J. Appl. Mech. 38 (1971) 729–738.
[6] A.S. Grove, F.H. Shair, E.E. Petersen, A. Acrivos, An experimental investigation of the steady separated flow past a circular cylinder, J. Fluid Mech. 19 (1964) 60–80.
[7] M. Konig, B.R. Noack, H. Eckelmann, Discrete shedding modes in the von Karman Vortex street, Phys. Fluids A 5 (1993) 1846.
[8] M.C. Lai, C.S. Peskin, An immersed boundary method with formal second-order accuracy and reduced numerical viscosity, J. Comp. Phys. 160 (2000) 705–719.
[9] C. Liu, X. Zheng, C.H. Sung, Preconditioned multigrid methods for unsteady incompressible flows, J. Comp. Phys. 139 (1998) 35–57.
[10] R. Mittal, Planar symmetry in the unsteady wake of a sphere, AIAA J. 37 (1999) 388–390.
[11] J. Mohd-Yusof, Interaction of Massive Particles with Turbulence, Ph.D. Dissertation, Dept. of Mechanical and Aerospace Engineering, Cornell Univ., 1996.
[12] J. Mohd-Yusof, Combined immersed-boundary/B-spline methods for simulations of flow in complex geometries, Annual Research Briefs, Center for Turbulence Research, 1997, 317–327.
[13] C.S. Peskin, Flow patterns around heart valves: A numerical method, J. Comp. Phys. 10 (1972) 252–271.
[14] C.S. Peskin, The immersed boundary method, Acta Numer. 11 (2002) 479–517.
[15] J.F. Ravoux, A. Nadim, H. Haj-Hariri, An embedding method for bluff body flows: Interactions of two side-by-side cylinder wakes, Theoret. Comput. Fluid Dyn, 16 (2003) 433–466.
[16] A. Roshko, On the development of turbulent wakes from vortex streets, NACA Report 1191 (1954) 1–25.
[17] E.M. Saiki, S. Biringen, Numerical simulation of a cylinder in uniform flow: Application of a virtual boundary method, J. Comp. Phys. 123 (1996) 450–465.
[18] A.L.F. Lima E Silva, A. Silveira-Neto, J.J.R. Damasceno, Numerical simulation of two-dimensional flows over a circular cylinder using the immersed boundary method, J. Comp. Phys. 189 (2003) 351–370.
[19] P.N. Swarztrauber, R.A. Sweet, Algorithm 541, Efficient FORTRAN subprograms for the solution of separable elliptic partial differential equations [D3], ACM Trans. on Math. Software 5 (1979) 352–364.
[20] A.-K. Tornberg, B. Engquist, Numerical approximations of singular source terms in differential equations, J. Comp. Phys. 200 (2004) 462–488.
[21] Y.H. Tseng, J.H. Ferziger, A ghost-cell immersed boundary method for flow in complex geometry, J. Comp. Phys. 192 (2003) 593–623.
[22] R. Verzicco, J. Mohd-Yusof, P. Orlandi, D. Haworth, Large eddy simulation in complex geometric configurations using boundary body forces, AIAA J. 38 (3) (2000) 427–433.
[23] M.M. Zdravkovich, Flow Around Circular Cylinders, Oxford University Press, 1997.
[24] H.Q. Zhang, U. Fey, B.R. Noack, M. Konig, H. Eckelmann, On the transition of the cylinder wake, Phys. Fluids 7 (4) (1995) 165–189.